

AI-supported Degradation Study of Carbon-based Perovskite Solar Cells, Learning the Device Physics of Perovskite Solar Cells: A Drift-Diffusion-Guided Autoencoder Approach

Oliver Zbinden, Sharun Parayil Shaji, Wolfgang Tress

Abstract

Carbon-electrode-based PSC devices are stressed under 1 Sun equivalent illumination in a stability setup, and different scan-speed dependent current-voltage (J-V) curves are measured during aging. The collected data is used to estimate several physical parameters that contain information about charge transport and recombination using Machine Learning (ML), which allows for in situ tracking of possible signs of degradation. These results are compared to what can be classically interpreted by analysing changes in J-V curves, and the evolution of the predicted parameters is studied. The predictions are then used to simulate a digital twin of the measured devices, and their physical implications and the differences between measurements and devices are discussed.

1 Introduction

Since their invention [1], perovskite solar cells (PSCs) have experienced an impressive increase in efficiency from 3.8% to almost 27% [2], which is only 0.3% behind silicon solar cells. The record for carbon-based PSCs recently reached 23.2% [3]. Still, some problems have to be overcome, most importantly, degradation. Despite huge progress in understanding the underlying mechanisms [4–12] and improvements [13–18], these problems are still not fully solved. Regarding stability and degradation, most studies using Artificial Intelligence (AI) focused on overall device performance, such as predicting the evolution of power conversion efficiency (PCE) over time [19–21], or the time it takes for PCE to drop to 80% of its initial value, T_{80} [22–25]. This is very helpful for predicting the lifetime of a device and for quality control. However, these applications do not directly contribute to the improvement of PSCs or identify sources of PCE loss. ML has recently been shown to provide reliable estimations of device parameters based on J-V curve measurements [26]. This approach allows for the estimation of parameters of devices, for example, to improve the accuracy of measurement matching simulation.

In this paper it is demonstrated how ML can be used to track parameter changes that cannot be directly

measured during stressing the devices without interruptions, such as transfer to different measurement setups. Two devices from *Solaronix* [27] are kept in a stability setup inside inert atmosphere with constant illumination for a total of 23 days, one device under maximum power point (MPP) tracking, and the other device under open circuit voltage (V_{OC}) tracking. Two additional unstressed devices were kept as references. Stressing devices in such a way is likely to cause degradation [28, 29]. The tracking is interrupted periodically and J-V curves are measured every day. With measured J-V curves, ML is used to estimate several physical parameters, allowing for tracking their evolution over time. 1D drift-diffusion (DD) device simulation allows a comparison between the measured J-V curves and a model with the obtained parameter estimates. The evolutionary trend of each parameter series is discussed and analyzed, based on the influence of possible degradation effects.

2 Methods

The simulation and ML architecture are adopted from [26]. For this study, the same training protocol is used.

2.1 Device Simulation

Starting with a carbon electrode-based mesoporous metal-oxide-perovskite based [30, 31], with an FTO/TiO₂/m-TiO₂-MAPI/m-ZrO₂-MAPI/Carbon structure (Figure 1), several material parameters are varied randomly, each of them independently. The varied parameters are the surface recombination velocity between the mesoporous perovskite-TiO₂ and TiO₂ layer $S_{e, top}$, $S_{h, top}$, in the mesoporous perovskite-metal oxide layers electron and hole mobilities μ_e , μ_h , electron and hole recombination lifetimes τ_e , τ_h , anion and cation densities ρ_A , ρ_C , electron mobility in TiO₂ μ_{TiO_2} , and cation mobilities μ_C . These parameters are selected based on their influence on the device, in order to cover various phenomena, such as changes related to charge transport vs. charge recombination, or electronic vs. ionic effects. These parameters are expected to show

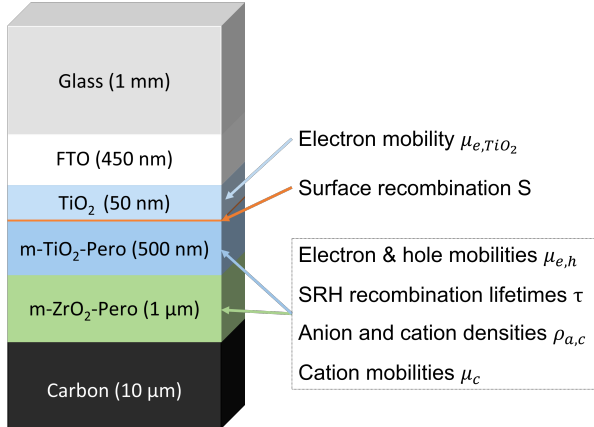


Figure 1: Illustration of the device stack of the mesoporous PSCs used in experiment and simulation. The arrows indicate the layers where parameters were varied.

Table 1: Literature-oriented parameter range for the different quantities, based on physically reasonable boundaries. Cation mobilities μ_C were only varied in the transient case.

Param.	Minimum	Maximum	Units
S	10^{-3}	100	cm/s
μ	10^{-2}	10^3	cm ² /Vs
τ	1	10^4	ns
μ_{TiO_2}	$2.5 \cdot 10^{-5}$	1	cm ² /Vs
ρ_{Ion}	10^{14}	10^{20}	cm ⁻³
μ_C	10^{-15}	10^{-4}	cm ² /Vs

some sort of variability between individual devices, influenced by different conditions during fabrication, or caused by material changes during degradation [32–34]. To reduce the complexity of the DD model, we set $\mu_e = \mu_h =: \mu$, $S_{e,top} = S_{h,top} =: S$, $\tau_e = \tau_h =: \tau$, and $\rho_A = \rho_C =: \rho_{Ion}$. Note especially that the parameters in the m-TiO₂-MAPI and m-ZrO₂-MAPI layers are assumed to be the same regarding charge transport and recombination, they only differ in their optical and light absorption properties. Because most reported parameters are determined for pure perovskite layers (for example in [35]), there is only little information for mesoporous perovskite-metal-oxide materials [30]. Therefore, the ranges within the parameters are varied are relatively wide, but still within physically reasonable boundaries, as listed in Table 1.

This wide range of varied parameters leads to simulated J-V curves that cover a space reaching from a sample that can be considered as completely degraded, up to a hypothetical device that outperforms the measured devices. This introduces a good amount of generalizability, which is needed for ML training. To detect the influence of mobile ions, different scan speeds are simulated (0.005, 0.05, 0.5, 5,

50, 100) V/s in decreasing order, first in forward, then in reverse direction (0 V - 1.2 V - 0 V).

2.2 ML Model Description

The encoder part of the AE consists of two convolutional and three dense layers, the decoder is mirror-symmetric. To find the parameters of interest, the loss function consists of two terms. The first term compares the input, the simulated J-V curves, to the AE output, the reconstructed J-V curves. The second additional term in the loss function, which can be seen as a condition, compares the true parameter values of the training data known from simulation, both terms are weighted equally. The second term in the loss function is crucial for two reasons. First, a normal AE undercomplete compresses the input in a way that retains necessary information to reconstruct the input, but in a "black-box" way. It could not be verified that the latent parameters indeed contain information of the parameters varied in simulation, and, if so, the function that maps the latent parameters to the physical parameters would be unknown. Second, assuming that the simulation parameters are mapped to the latent space independently without convoluting parameters, the order of parameters in the latent vector would be unknown, with $6! = 720$ possible combinations for the given task with 6 differently varied parameters.

The input of the AE is a 1D array with length 732 that consists of the simulated or measured current values in increasing order of scan speeds starting with the forward direction, interpolated to 0.02 V steps. The current arrays are normalised with the global minimum and maximum from the simulated data. The six varied parameters, S , μ , τ , μ_{TiO_2} , μ_C , and ρ_{Ion} are collected in a 1D array for each simulated device, and log-normalised with the respective global minimum and maximum known from simulation. In total, there are 50'000 simulated devices that are split into fractions of 70 : 15 : 15 for training, validation, and test sets. Training is performed in a 10-fold cross-validation.

After training is completed, the encoder and decoder parts can be used independently. The decoder can act as a fast surrogate device simulator, but this part of the AE is discarded since, for parameter estimation, only the encoder is needed.

2.3 Device Measurement

J-V measurements were performed using a PAIOS system (Fluxim AG) under simulated AM1.5G illumination (Oriel Sol3A Class ABB, model 94011A). Encapsulated devices were preconditioned under one sun illumination at open-circuit voltage for 5 minutes prior to the J-V measurements. Subsequently, J-V curves were recorded sequentially at scan rates

of 100, 50, 5, 0.5, 0.05, and 0.005 V/s, in that order, without intermediate light soaking or voltage preconditioning. For each scan rate, the measurement was performed first in the forward direction (from short-circuit to open-circuit voltage), followed by the reverse direction. All measurements were carried out in ambient atmosphere.

Light-intensity dependent J-V measurements at scan speed of 0.036 V/s were also performed using PAIOS by varying the illumination (White LED) intensity from aprox. 2 to 0.02 sun equivalent intensity to analyze recombination behaviour and extract ideality factors.

Stressing of the cells was done under MPP and V_{oc} with white led (Colour temperature = 5000K) illumination of one sun equivalent by employing Maximum power point tracker (MP0205M24 from LPVO) . During the stressing we measured the J-V as mentioned above using the potentiostat EmStat-4s HR from PalmSense.

3 Results

The devices subjected to stress (SN112 at MPP and SN114 at V_{oc}) exhibited clear signs of degradation. SN112 retained 90% of its initial power conversion efficiency after aging (Figure 2 a), while SN114, which was held at V_{oc} , showed a reduction in open-circuit voltage from 0.88 V to 0.84 V. The devices were sufficiently aged to ensure that degradation processes occurred within their operational regime. As shown in Figure 2 b, distinct spikes in V_{oc} appear immediately after each J-V measurement. These transients are attributed to changes in the ionic distribution, consistent with observations reported in Reference [36], and the resulting ionic losses are also reflected in the J-V curves in Figures 9 & 10. The J_{SC} shows scan rate-dependent behaviour, where the losses are more prominent in the fastest scans. This can also be seen as the spikes in Figure 2 b.

Before the parameter estimates from the encoder are discussed, the behaviour of V_{OC} , J_{SC} , FF, hysteresis and the series resistance of the measured J-V curves are analyzed and discussed. Figures 3 & 7 a, d show that V_{OC} decreased over time for both devices similarly, but showing an increasing tendency for the last ≈ 50 hours. V_{OC} is scanning direction dependent in all cases, but less pronounced at higher scan speeds, as expected. The behaviour of J_{SC} in the devices is not exactly the same, even though the end result is similar. It decreased in magnitude for both devices when the first and last days are compared for most scan speeds, but there are notable differences in between. The device that was kept at V_{OC} experienced a rather steep decrease of J_{SC} (Figures 3 & 7 b) at the beginning, for all scan speeds, except the slowest two (0.05 V/s & 0.005 V/s), with a trend that indicates some sort of saturation. The

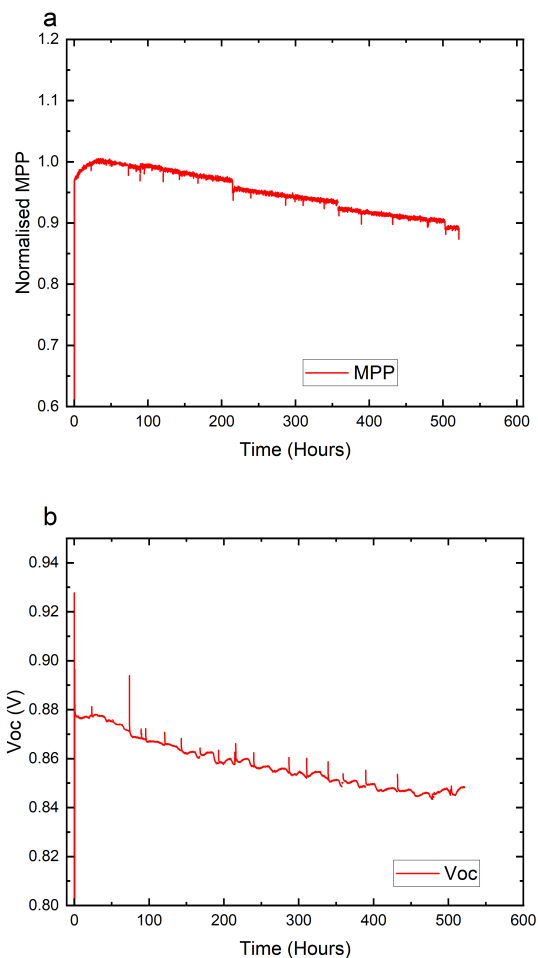


Figure 2: Aging data for devices SN112 and SN114, stressed under MPP and V_{OC} , respectively. Both devices were aged for over 550 hours (23 days).

0.05 V/s scans still show the same trend, but always at higher currents. There is almost no change in J_{SC} for the 0.005 V/s. Scanning direction dependencies of J_{SC} only seem to be present for (0.05, 0.5, 5) V/s, not for (0.005, 50, 100) V/s. On the other hand, the device kept under MPP first experienced an increase in J_{SC} before they decreased as well (Figures 3 & 7 b), except for the 0.005 V/s and 0.05 V/s cases. The slowest scan speed shows an improvement of J_{SC} over time without scan speed dependence, and the 0.05 V/s measurements are relatively stable. The FFs show similar trends of a slight decrease over time for both devices (Figures 3 & 7 c, f). The difference between forward and reverse scan is almost negligible for the fastest scan speeds, and very prominent for the slowest ones, which is explained by the differences in V_{OC} . The picture for 0.5 V/s is somewhat inconclusive for both devices, because the forward scan follows the trend of the faster scans with only slightly decreased FF.

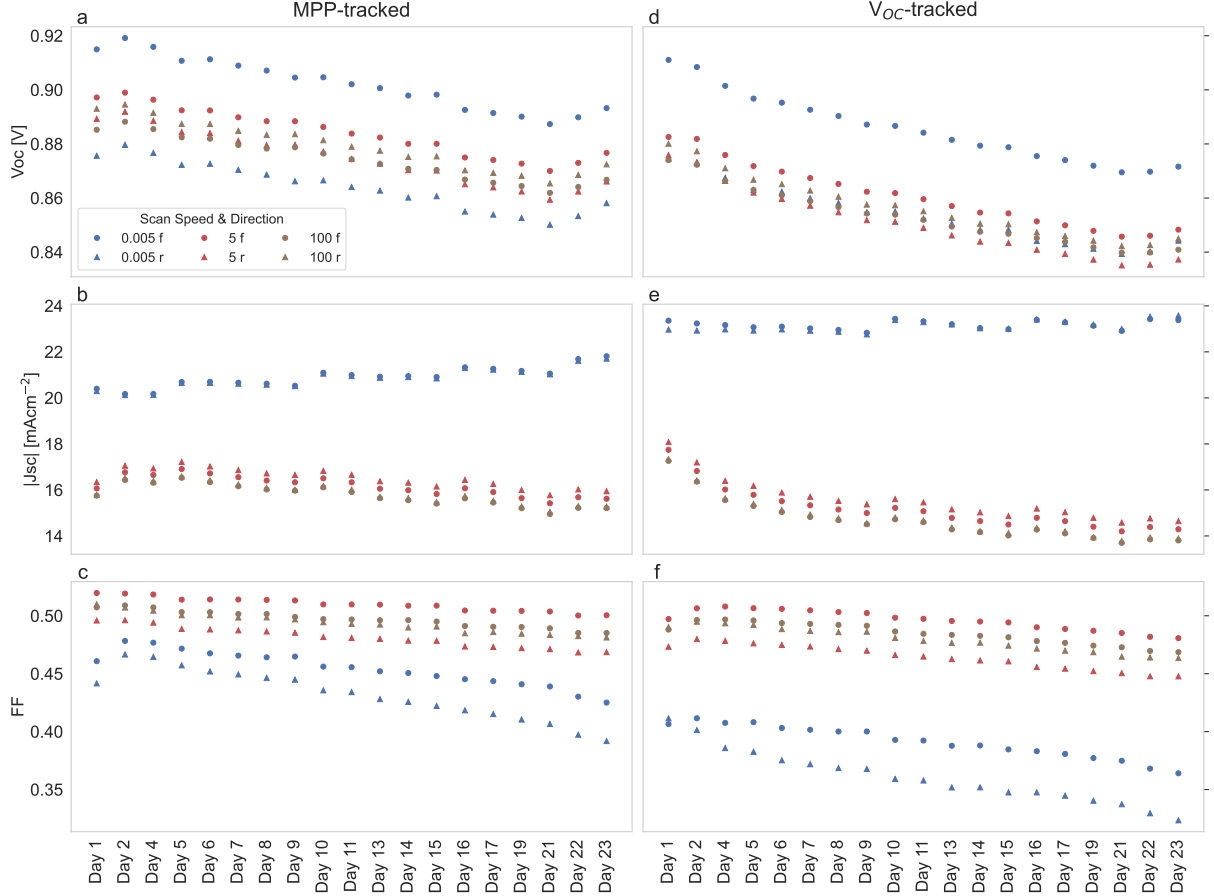


Figure 3: Evolution of key parameters for the two devices in the stability setup for a selection of the scan speeds. a-c show the results for the device kept at MPP, d-f for the device kept at V_{OC} . a & d: V_{OC} . b & e: Absolute value of J_{SC} . c & f: FF. Figure 7 shows the full data for all scan speeds.

Due to ionic charge redistribution, hysteresis can be observed in PSCs [37–39], which can also be seen in Figures 9 & 10 for the scan speeds (0.005 – 5) V/s. This hysteresis is oftentimes reported with a dimensionless hysteresis index that quantifies the difference between forward and reverse scan, for example by $\frac{\text{reverse PCE} - \text{forward PCE}}{\text{reverse PCE}}$. A positive index, with higher currents in reverse direction, is normal, a negative index inverted hysteresis. This definition can be problematic when one wants to quantify the behaviour of J-V curves that show both, normal and inverted hysteresis at different voltages, because the effect partially cancels out. This can be observed in both devices at the scan speed 0.05 V/s (Panel b in Figures 9 & 10). Figure 4 therefore shows two different hysteresis indices, panel a is the hysteresis based on PCE, panel b the hysteresis from the area difference of the J-V curves. Both representations have advantages and disadvantages. Panel a contains information about normal or inverted hysteresis, but only for one point, and panel b shows the absolute area between the forward and reverse scan, but does not reveal if hysteresis is inverted or not. The scan speeds (0.05, 50, 100) V/s show almost no hysteresis in panel a. This is consistent

with the results in panel b for the fast scan speeds, but as already indicated, not for 0.05 V/s.

In the cases of the fast scan speeds, this indicates that they are already too fast to resolve ionic effects, but for 0.05 V/s, the result is inconclusive. For the other scan speeds, hysteresis is always inverted, increasing in magnitude over time. Both devices show very similar trends. The only outlier is the slowest scan speed, where the difference between MPP and V_{OC} tracked devices is more notable. However, the changes are still not dramatic as can be seen in Figures 9, 10.

Summarizing the discussed findings, it can be said that when stressing these devices, in both cases, V_{OC} changes notably. J_{SC} also decreases substantially for most scan speeds when the device is kept at V_{OC} , but it is relatively stable under MPP tracking. FF tends to decrease with time, but not substantially. Different scan speeds show different trends, as mentioned before, which is not easy to quantify consistently when we have multiple scan speeds. For single J-V curves, like steady state, a discussion of the influence of different parameters can be found in literature [40, 41] (in the respective SI). Of course, not every possible parameter is varied there, so it

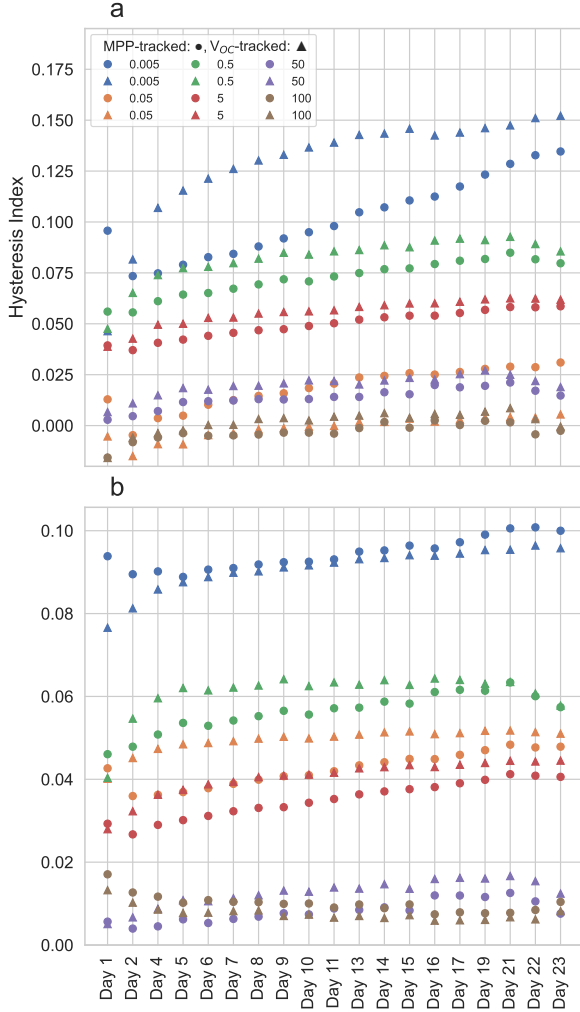


Figure 4: Two different ways to determine hysteresis. a: Hysteresis (PCE). b: Ratio of difference in area of J-V curves at each scan speed.

may be possible that other changes could lead to such a change in the J-V curve as well. Also note that there are differences between the carbon-based device here to the planar architecture simulated in [40, 41], but the influence of parameter changes is basically the same. Out of all the parameters discussed, there are only a few that show the behaviour observed in the studied devices. These parameters are predominantly related to recombination, in the bulk or at the surface. In principle, these changes can, to some extent, be explained by changes in ion densities as well. Since the influence on the J-V curve can depend on the ion species [41], which was not included in the simulation originally used to train the AE ($\rho_A = \rho_C$), this is not covered by the AE model. Based on this information, it is expected that, if the AE estimates the parameters reasonably, the most notable changes should be related to recombination.

The AE-based parameter estimates inferred from the J-V curves measured while the devices were stressed

are shown in Figure 5 and Table 3. These results are now interpreted and, where possible, supported with different characterization measurements before and after stressing the devices.

S: The surface recombination velocity increases over time for both devices, and it seems that it approaches a value of around 50 cm/s for the device kept at MPP and around 100 cm/s for the device kept at V_{OC} . The initial difference of the parameter estimates for the two devices shows some amount of sample variation, which can be seen in the J-V curves as well. The changes over time are not the same, which could be related to the different stressing conditions. Light-intensity-dependent J-V measurements were performed to extract the experimental ideality factor, which was further compared with the values obtained from drift-diffusion simulations using parameters estimated by the autoencoder model as depicted in Figure 12. While the simulated ideality factors, derived from AE-parameterised drift-diffusion modelling, reproduce the qualitative trend of the measurements, their absolute values are smaller, which may arise from the neglect of ionic redistribution and associated field screening effects that enhance recombination in real devices [42].

μ_{pero} : As no significant decrease in μ_{TiO_2} is observed, while the series resistance shows a consistent rise over time, it is reasonable to attribute the emerging transport limitations to changes within the perovskite layer. Although the V_{OC} of these devices does not appear to be bulk-limited, the evolution of the series resistance aligns closely with μ of the device aged under MPP conditions. The device aged under Voc exhibits a similar trend up to day 9, after which the alignment diverges (see Figure 16). These effects are likely not related to μ_{pero} , but will be discussed in the section about ions. Notably, by this stage, the extracted *S* parameter exceeds the range represented in the AE model’s training dataset, indicating that the system has entered a regime not captured during model development.

τ : For the device kept at MPP, τ is, initially, within the same order of magnitude with what was obtained from TrPL, which was fitted assuming a double exponential decay. Both devices had decay time constants of 1.47 ns and 1.39 ns, respectively. These values are in agreement with what was measured elsewhere [3]. However, inferring τ from transient photovoltage (TPV) measurement, the results are several orders of magnitude higher, which is often-times the case in PSCs [3, 43]. These measured effective lifetimes account for various effects, including bulk and surface recombination. The capacitive and ionic properties of the device dominate the measurements of TPV [44, 45]. The initially estimated low lifetimes can be explained by the mesoporous structures infiltrated with perovskite, leading to a bulk that is effectively one big interface with presumably high defect densities at these surfaces. For

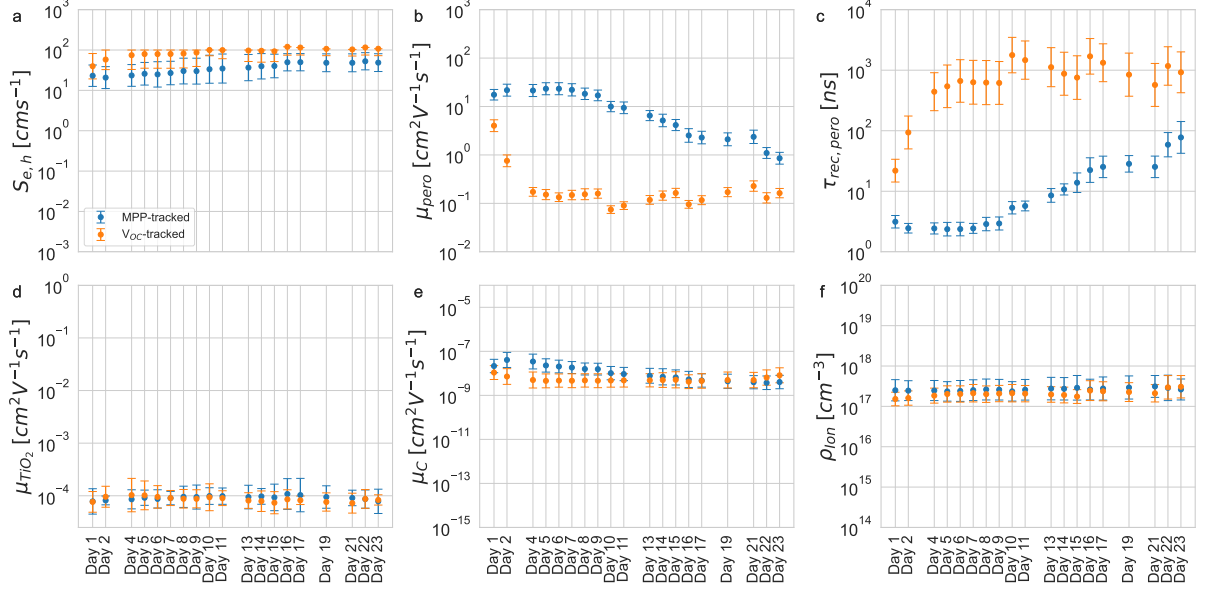


Figure 5: Evolution of AE-estimated parameters, based on the J-V curves measured on each day. Uncertainties are estimated based on the mean difference between true parameter values of the test set in Figure 8 and their estimates in an interval of ± 0.02 for each predicted device parameter estimate.

the device kept at V_{OC} , τ is already higher from the beginning, and increases to values that are more comparable to reported lifetimes based on TPV measurements. From Figure 8, it can be seen that the AE predictions are more reliable at shorter lifetimes, because if τ is longer than the (extreme) time needed for extraction, it does not affect the J-V curve anymore, which is indicated by larger error bars in Figure 5. Due to the significant differences between lifetimes depending on the measurements they are based on, it is difficult to tell which method is closer to reality. It is therefore challenging to tell if the predictions are correct.

μ_{pero} & $\tau_{rec, pero}$: These two parameters are also discussed together because the product is closely related to the diffusion length $L = \sqrt{D\tau} = \sqrt{\mu\tau \frac{k_B T}{q}}$. The product $\mu\tau$ mainly influences J_{SC} , and, if S dominates, the effects of τ are suppressed. For the device kept at MPP, the AE estimates show a decrease of μ_{pero} and an increase of $\tau_{rec, pero}$ of around the same order of magnitude, leading to a constant product $\mu \cdot \tau$ (Figure 6), closely following J_{SC} of the slowest scan speed in Figure 3b. The results for the V_{OC} -tracked device are not as conclusive on first sight because the measured J_{SC} (Figures 3 & 7 e) is constant over time and does not follow the behaviour shown if Figure 6.

μ_{TiO_2} : These parameter estimates are very similar for both devices and constant over time, changes only occur within the calculated uncertainties. It seems that μ_{TiO_2} is not affected by this type of stress. Such behaviour is consistent with the relatively stable nature of the compact μ_{TiO_2} layer, where electron transport is governed by trap-limited diffusion [46].

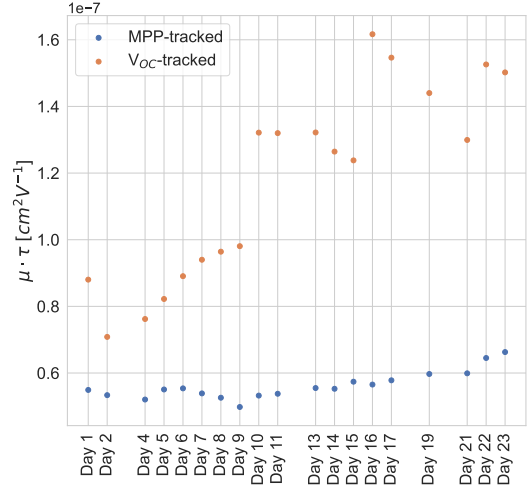


Figure 6: The evolution of $\mu\tau$ is shown in this figure, complementary to the discussion and Figure 5.

Note that only slight changes of μ_{TiO_2} can already influence the J-V curve substantially. Consequently, simulation based on the estimated parameters can agree much better with the measurement if μ_{TiO_2} is varied only within the uncertainty range.

μ_C & $\rho_{A,C}$: Overall, it seems that there is not much change in the ionic parameters. It seems that for the device kept at MPP, μ_C decreases slightly. The changes are within the indicated uncertainties, or just slightly outside. For the device kept at V_{OC} , the variation in μ_C is within uncertainty over all 23 days. For both devices, changes of $\rho_{A,C}$ are within uncertainty, indicating approximately constant ion

densities. However, it seems that the operational bias at V_{OC} accelerates the series resistance increase, likely due to accumulation of ions at the interface, leading to FF loss [47]. The behaviour of these parameters during the experiment, especially μ_C , is supported by the hysteresis that is not much affected (Figure 4), and the small estimated changes in the J-V measurements (Figures 9, 10) could already indicate that μ_C is indeed not exactly constant over time. Comparing the J-V curves from the first and last day of the study (Figures 9, 10), it can be seen that the shapes of the J-V curves are not much affected. A quantitative verification of the ionic density is not possible from impedance spectroscopy, since the plateau at lower frequencies in the capacitance-frequency (C-f) plot (Figure 11) that corresponds to the ionic capacitance[48] could not have been reached. But there is no significant change in the C-f plot before and after stressing, which points to minimal variation in ion density. This agrees with the ionic density estimates we get from the AE.

The estimated parameters can be used as simulation input to compare measurements and simulations. For the device kept at MPP, the model agrees initially, slightly overpredicting the current and FF. These differences are approximately constant for the first 9-11 days, depending on the scan speed. As time passes, the differences between the measurements and simulations increase, where the scan speeds (0.005, 0.05, 50, and 100) V/s do not show hysteresis in simulation, and the deviations are consistent for these scan speeds. For 0.5 V/s and 5 V/s, the results are a bit different. For 0.5 V/s, the current matches the experiment in forward much better between MPP and V_{OC} , but overpredicts the current between MPP and J_{SC} . At 5 V/s, the simulation matches the measurement almost perfectly throughout the 23 days. On the other hand, with increasing time, the difference between the measurement and simulation of the reverse scanning direction increases for these two scan speeds, current and FF are overpredicted, as in the other cases. With higher scan speeds, V_{OC} is also estimated to be too high. The trends in the simulations for the device kept at V_{OC} are very similar, but they are more pronounced. These differences indicate that the estimated values or the underlying DD model are not as close to the real devices as intended, and there are several possible reasons for this. Consulting the literature again to discuss the J-V curves [40, 41], these differences can be explained by changes in ion densities or parameters related to recombination in the bulk or at the surface. These two different possibilities are discussed separately. It has recently been found that ionic effects are the dominating factor of light-induced degradation of PSCs [47]. There, it has been shown that recombination in the bulk and at the surface depends on

ion density, with a stronger influence on the surface recombination. The result, lower current and FF, is one mechanism that can change the simulated J-V curves towards what was measured. But why do the results not match? The AE could estimate higher ion densities and possibly solve the problem, but it does not. Why? Cations accumulate near the carbon-perovskite interface, causing recombination. The behaviour of this effect in a planar device, as simulated, is very different compared to the actual mesoporous structure. Furthermore, in a real device, the mobile ions move through the different layers filled with perovskite, in this case the two mesoporous TiO_2 and ZrO_2 , as well as partially the carbon layer. The mesoporous TiO_2 -perovskite layer is, effectively, one big surface, which cannot be simulated in a one-dimensional DD model for obvious reasons.

4 Discussion

In this study, it has been demonstrated that AEs can be used to track device changes during degradation on a fundamental level. Two carbon-based PSCs were stressed for 23 days under light, one was kept at MPP, the other at V_{OC} in order to provoke degradation. While the device kept at MPP only changes slightly, the device kept at V_{OC} shows much stronger signs of degradation, especially with regard to J_{SC} . Based on the evolution of V_{OC} , J_{SC} , and FF, it was discussed what quantities most likely changed based on classical J-V curve analysis. The AE was trained to predict different material parameters from J-V curves as an input, and, based on the J-V curves measured during aging the devices under examination, estimated and evolution of physical parameters which is in agreement with what was expected classically. The results are, where possible, supported by additional measurements.

The parameter estimates obtained from PAIOS measurements, listed in Table 2, where the devices were illuminated under a calibrated solar simulator, show noticeable deviations from those extracted during device stressing under white LED illumination. When these PAIOS-derived parameters are used in the DD simulations, the simulated J-V characteristics exhibit a significantly better agreement with the experimentally measured J-V curves (Figures 14 & 15). The discrepancies between the two sets of measurements likely originate from differences in the illumination spectra and associated photo-generation profiles, and the consequences associated with this, as well as from variations in contact resistance, and parasitic capacitances between the two setups. The model training was done with the simulations which used the solar spectra, hence the parameters extracted from the PAIOS measurements appear physically more consistent and yield quantitatively accu-

Table 2: Parameter estimations from the Paios measurements before and after aging.

		S [cm s^{-1}]	μ [cm $^2V^{-1}s^{-1}$]	τ [ns]	μ_{TiO_2} [cm $^2V^{-1}s^{-1}$]	μ_C [cm $^2V^{-1}s^{-1}$]	ρ_{ton} [cm $^{-3}$]
REFERENCE 1	BEFORE	2.84	13.32	4.16	$3.57 \cdot 10^{-5}$	$1.12 \cdot 10^{-7}$	$1.82 \cdot 10^{17}$
	AFTER	$9.85 \cdot 10^{-3}$	19.26	10.09	$7.89 \cdot 10^{-5}$	$2.12 \cdot 10^{-5}$	$1.11 \cdot 10^{17}$
REFERENCE 2	BEFORE	$5.33 \cdot 10^{-1}$	12.88	3.87	$3.59 \cdot 10^{-5}$	$9.30 \cdot 10^{-8}$	$1.79 \cdot 10^{17}$
	AFTER	$1.21 \cdot 10^{-3}$	15.33	8.93	$8.06 \cdot 10^{-5}$	$4.60 \cdot 10^{-5}$	$2.47 \cdot 10^{17}$
MPP-TRACKED	BEFORE	5.98	16.21	6.71	$3.64 \cdot 10^{-5}$	$1.10 \cdot 10^{-7}$	$1.00 \cdot 10^{17}$
	AFTER	52.03	$6.47 \cdot 10^{-1}$	$1.74 \cdot 10^2$	$5.85 \cdot 10^{-5}$	$2.03 \cdot 10^{-8}$	$1.15 \cdot 10^{17}$
V _{OC} -TRACKED	BEFORE	12.79	11.93	4.30	$3.85 \cdot 10^{-5}$	$6.25 \cdot 10^{-8}$	$1.17 \cdot 10^{17}$
	AFTER	67.86	$4.21 \cdot 10^{-1}$	$2.16 \cdot 10^2$	$5.62 \cdot 10^{-5}$	$6.28 \cdot 10^{-9}$	$1.32 \cdot 10^{17}$

rate reproductions of the J-V behaviour. Therefore, these parameters are considered more reliable.

Although the drift-diffusion simulations used to train the AE are based on a one-dimensional approximation, the experimental device employs a mesoporous scaffold, where recombination and transport occur over an extended interfacial area. The increased apparent S predicted by the AE may therefore represent an effective parameter capturing both interfacial degradation and geometric enhancement of recombination pathways inherent to the porous structure.

The parameter estimates can be used as a starting point to refine device simulation, which can contribute to a deeper understanding of a device and push the technology further to more stable and efficient devices.

References

- [1] A. Kojima, K. Teshima, Y. Shirai, and T. Miyasaka, "Organometal Halide Perovskites as Visible-Light Sensitizers for Photovoltaic Cells," *Journal of the American Chemical Society*, vol. 131, no. 17, pp. 6050–6051, May 2009, publisher: American Chemical Society. [Online]. Available: <https://doi.org/10.1021/ja809598r>
- [2] NREL, "Best Research-Cell Efficiency Chart plotted by National Renewable Energy Laboratory, USA," <https://www.nrel.gov/pv/interactive-cell-efficiency.html>, visited on 23.04.2025.
- [3] Y. Ma, J. Liu, X. Chen, X. Zhao, J. Qi, B. She, S. Liu, Y. Jiang, Y. Sheng, C. Han, G. Zhang, J. Xie, K. Chen, Y. Cheng, J. Xiang, L.-M. Yang, Y. Zhou, F. Ling, Y. Zhou, A. Mei, and H. Han, "Enhancing hole-conductor-free, printable mesoscopic perovskite solar cells through post-fabrication treatment via electrophilic reaction," *Nature Energy*, Aug. 2025. [Online]. Available: <https://doi.org/10.1038/s41560-025-01823-8>
- [4] A. M. A. Leguy, Y. Hu, M. Campoy-Quiles, M. I. Alonso, O. J. Weber, P. Azarhoosh, M. van Schilfgaarde, M. T. Weller, T. Bein, J. Nelson, P. Docampo, and P. R. F. Barnes, "Reversible Hydration of CH₃NH₃PbI₃ in Films, Single Crystals, and Solar Cells," *Chemistry of Materials*, vol. 27, no. 9, pp. 3397–3407, May 2015, publisher: American Chemical Society. [Online]. Available: <https://doi.org/10.1021/acs.chemmater.5b00660>
- [5] B. Conings, J. Drijkoningen, N. Gauquelin, A. Babayigit, J. D'Haen, L. D'Olieslaeger, A. Ethirajan, J. Verbeeck, J. Manca, E. Mosconi, F. D. Angelis, and H.-G. Boyen, "Intrinsic thermal instability of methylammonium lead trihalide perovskite," *Advanced Energy Materials*, vol. 5, no. 15, p. 1500477, 2015. [Online]. Available: <https://advanced.onlinelibrary.wiley.com/doi/abs/10.1002/aenm.201500477>
- [6] D. Bryant, N. Aristidou, S. Pont, I. Sanchez-Molina, T. Chotchunangatchaval, S. Wheeler, J. R. Durrant, and S. A. Haque, "Light and oxygen induced degradation limits the operational stability of methylammonium lead triiodide perovskite solar cells," *Energy Environ. Sci.*, vol. 9, pp. 1655–1660, 2016. [Online]. Available: <http://dx.doi.org/10.1039/C6EE00409A>
- [7] Y. Li, X. Xu, C. Wang, B. Ecker, J. Yang, J. Huang, and Y. Gao, "Light-Induced Degradation of CH₃NH₃PbI₃ Hybrid Perovskite Thin Film," *The Journal of Physical Chemistry C*, vol. 121, no. 7, pp. 3904–3910, Feb. 2017, publisher: American Chemical Society. [Online]. Available: <https://doi.org/10.1021/acs.jpcc.6b11853>
- [8] N. Aristidou, I. Sanchez-Molina, T. Chotchuangchutchaval, M. Brown, L. Martinez, T. Rath, and S. A. Haque, "The role of oxygen in the degradation of methylammonium lead trihalide perovskite photoactive layers," *Angewandte Chemie International Edition*, vol. 54, no. 28, pp. 8208–8212, 2015. [Online]. Available: <https://onlinelibrary.wiley.com/doi/abs/10.1002/anie.201503153>

- [9] M.-c. Kim, N. Ahn, E. Lim, Y. U. Jin, P. V. Pikhitsa, J. Heo, S. K. Kim, H. S. Jung, and M. Choi, "Degradation of $\text{CH}_3\text{NH}_3\text{PbI}_3$ perovskite materials by localized charges and its polarity dependency," *J. Mater. Chem. A*, vol. 7, pp. 12075–12085, 2019. [Online]. Available: <http://dx.doi.org/10.1039/C9TA03180D>
- [10] D. Lin, Y. Gao, T. Zhang, Z. Zhan, N. Pang, Z. Wu, K. Chen, T. Shi, Z. Pan, P. Liu, and W. Xie, "Vapor deposited pure a-fapbi3 perovskite solar cell via moisture-induced phase transition strategy," *Advanced Functional Materials*, vol. 32, no. 48, p. 2208392, 2022. [Online]. Available: <https://advanced.onlinelibrary.wiley.com/doi/abs/10.1002/adfm.202208392>
- [11] D. Di Girolamo, N. Phung, F. U. Kosasih, F. Di Giacomo, F. Matteocci, J. A. Smith, M. A. Flatken, H. Köbler, S. H. Turren Cruz, A. Mattoni, L. Cinà, B. Rech, A. Latini, G. Divitini, C. Ducati, A. Di Carlo, D. Dini, and A. Abate, "Ion migration-induced amorphization and phase segregation as a degradation mechanism in planar perovskite solar cells," *Advanced Energy Materials*, vol. 10, no. 25, p. 2000310, 2020. [Online]. Available: <https://advanced.onlinelibrary.wiley.com/doi/abs/10.1002/aenm.202000310>
- [12] D. A. Jacobs, C. M. Wolff, X.-Y. Chin, K. Artuk, C. Ballif, and Q. Jeangros, "Lateral ion migration accelerates degradation in halide perovskite devices," *Energy Environ. Sci.*, vol. 15, pp. 5324–5339, 2022. [Online]. Available: <http://dx.doi.org/10.1039/D2EE02330J>
- [13] S. M. Kang, N. Ahn, J.-W. Lee, M. Choi, and N.-G. Park, "Water-repellent perovskite solar cell," *J. Mater. Chem. A*, vol. 2, pp. 20017–20021, 2014. [Online]. Available: <http://dx.doi.org/10.1039/C4TA05413J>
- [14] J. S. Yun, J. Kim, T. Young, R. J. Patterson, D. Kim, J. Seidel, S. Lim, M. A. Green, S. Huang, and A. Ho-Baillie, "Humidity-induced degradation via grain boundaries of $\text{HC}(\text{NH}_2)_2\text{PbI}_3$ planar perovskite solar cells," *Advanced Functional Materials*, vol. 28, no. 11, p. 1705363, 2018. [Online]. Available: <https://advanced.onlinelibrary.wiley.com/doi/abs/10.1002/adfm.201705363>
- [15] G. Grancini, C. Roldán-Carmona, I. Zimmermann, E. Mosconi, X. Lee, D. Martineau, S. Narbey, F. Oswald, F. De Angelis, M. Graetzel, and M. K. Nazeeruddin, "One-Year stable perovskite solar cells by 2D/3D interface engineering," *Nature Communications*, vol. 8, no. 1, p. 15684, Jun. 2017. [Online]. Available: <https://doi.org/10.1038/ncomms15684>
- [16] S. M. Park, M. Wei, J. Xu, H. R. Atapattu, F. T. Eickemeyer, K. Darabi, L. Grater, Y. Yang, C. Liu, S. Teale, B. Chen, H. Chen, T. Wang, L. Zeng, A. Maxwell, Z. Wang, K. R. Rao, Z. Cai, S. M. Zakeeruddin, J. T. Pham, C. M. Risko, A. Amassian, M. G. Kanatzidis, K. R. Graham, M. Grätzel, and E. H. Sargent, "Engineering ligand reactivity enables high-temperature operation of stable perovskite solar cells," *Science*, vol. 381, no. 6654, pp. 209–215, 2023. [Online]. Available: <https://www.science.org/doi/abs/10.1126/science.adi4107>
- [17] C. C. Boyd, R. Cheacharoen, K. A. Bush, R. Prasanna, T. Leijtens, and M. D. McGehee, "Barrier Design to Prevent Metal-Induced Degradation and Improve Thermal Stability in Perovskite Solar Cells," *ACS Energy Letters*, vol. 3, no. 7, pp. 1772–1778, Jul. 2018, publisher: American Chemical Society. [Online]. Available: <https://doi.org/10.1021/acseenergylett.8b00926>
- [18] Y. Zhao, J. Zhang, Z. Xu, S. Sun, S. Langner, N. T. P. Hartono, T. Heumueller, Y. Hou, J. Elia, N. Li, G. J. Matt, X. Du, W. Meng, A. Osvet, K. Zhang, T. Stubhan, Y. Feng, J. Hauch, E. H. Sargent, T. Buonassisi, and C. J. Brabec, "Discovery of temperature-induced stability reversal in perovskites using high-throughput robotic learning," *Nature Communications*, vol. 12, no. 1, p. 2191, Apr. 2021. [Online]. Available: <https://doi.org/10.1038/s41467-021-22472-x>
- [19] Çağla Odabaşı and R. Yıldırım, "Machine learning analysis on stability of perovskite solar cells," *Solar Energy Materials and Solar Cells*, vol. 205, p. 110284, 2020. [Online]. Available: <https://www.sciencedirect.com/science/article/pii/S0927024819306130>
- [20] J. Zhao, N. Rai, J. F. Benitez-Rodriguez, W. Yan, L. J. Sutherland, J. Yan, A. S. R. Chesman, J. Jasieniak, J. Lu, and U. Bach, "Cation optimization for bifacial surface passivation in efficient and stable perovskite solar cells," *EES Sol.*, vol. 1, pp. 56–65, 2025. [Online]. Available: <http://dx.doi.org/10.1039/D4EL00013G>
- [21] N. T. P. Hartono, H. Köbler, P. Graniero, M. Khenkin, R. Schlatmann, C. Ulbrich, and A. Abate, "Stability follows efficiency based on the analysis of a large perovskite solar cells ageing dataset," *Nature Communications*, vol. 14, no. 1, p. 4869, Aug. 2023. [Online]. Available: <https://doi.org/10.1038/s41467-023-40585-3>
- [22] P. Graniero, M. Khenkin, H. Köbler, N. T. P. Hartono, R. Schlatmann, A. Abate, E. Unger,

- T. J. Jacobsson, and C. Ulbrich, “The challenge of studying perovskite solar cells’ stability with machine learning,” *Frontiers in Energy Research*, vol. Volume 11 - 2023, 2023. [Online]. Available: <https://www.frontiersin.org/journals/energy-research/articles/10.3389/fenrg.2023.1118654>
- [23] I. Kouroudis, K. T. Tanko, M. Karimipour, A. B. Ali, D. K. Kumar, V. Sudhakar, R. K. Gupta, I. Visoly-Fisher, M. Lira-Cantu, and A. Gagliardi, “Artificial Intelligence-Based, Wavelet-Aided Prediction of Long-Term Outdoor Performance of Perovskite Solar Cells,” *ACS Energy Letters*, vol. 9, no. 4, pp. 1581–1586, Apr. 2024, publisher: American Chemical Society. [Online]. Available: <https://doi.org/10.1021/acseenergylett.4c00328>
- [24] M. Mammeri, H. Bencherif, L. Dehimi, A. Hajri, P. Sasikumar, A. Syed, and H. A. AL-Shwaiman, “Stability forecasting of perovskite solar cells utilizing various machine learning and deep learning techniques,” *Journal of Optics*, Apr. 2024. [Online]. Available: <https://doi.org/10.1007/s12596-024-01819-9>
- [25] W. A. Dunlap-Shohl, Y. Meng, P. P. Sunkari, D. A. C. Beck, M. Meilä, and H. W. Hillhouse, “Physiochemical machine learning models predict operational lifetimes of $\text{CH}_3\text{NH}_3\text{PbI}_3$ perovskite solar cells,” *J. Mater. Chem. A*, vol. 12, pp. 9730–9746, 2024. [Online]. Available: <http://dx.doi.org/10.1039/D3TA06668A>
- [26] O. Zbinden, E. L. Comi, E. Knapp, and W. Tress, “Autoencoder for parameter estimation and current-voltage curve simulation of perovskite solar cells,” *Research Square (preprint)*, 2025. [Online]. Available: <http://dx.doi.org/10.21203/rs.3.rs-8037624/v1>
- [27] Solaronix SA, <https://www.solaronix.com/>, visited on 12.12.2024.
- [28] W. Nie, J.-C. Blancon, A. J. Neukirch, K. Appavoo, H. Tsai, M. Chhowalla, M. A. Alam, M. Y. Sfeir, C. Katan, J. Even, S. Tretiak, J. J. Crochet, G. Gupta, and A. D. Mohite, “Light-activated photocurrent degradation and self-healing in perovskite solar cells,” *Nature Communications*, vol. 7, no. 1, May 2016. [Online]. Available: <https://doi.org/10.1038/ncomms11574>
- [29] K. Domanski, E. A. Alharbi, A. Hagfeldt, M. Grätzel, and W. Tress, “Systematic investigation of the impact of operation conditions on the degradation behaviour of perovskite solar cells,” *Nature Energy*, vol. 3, no. 1, pp. 61–67, Jan. 2018. [Online]. Available: <https://doi.org/10.1038/s41560-017-0060-5>
- [30] R. Kerremans, O. J. Sandberg, S. Meroni, T. Watson, A. Armin, and P. Meredith, “On the electro-optics of carbon stack perovskite solar cells,” *Solar RRL*, vol. 4, no. 2, p. 1900221, 2020. [Online]. Available: <https://onlinelibrary.wiley.com/doi/abs/10.1002/solr.201900221>
- [31] D. Bogachuk, R. Tsuji, D. Martineau, S. Narbey, J. P. Herterich, L. Wagner, K. Suginuma, S. Ito, and A. Hinsch, “Comparison of highly conductive natural and synthetic graphites for electrodes in perovskite solar cells,” *Carbon*, vol. 178, pp. 10–18, 2021. [Online]. Available: <https://www.sciencedirect.com/science/article/pii/S0008622321000300>
- [32] S. P. Dunfield, L. Bliss, F. Zhang, J. M. Luther, K. Zhu, M. F. A. M. van Hest, M. O. Reese, and J. J. Berry, “From defects to degradation: A mechanistic understanding of degradation in perovskite solar cell devices and modules,” *Advanced Energy Materials*, vol. 10, no. 26, p. 1904054, 2020. [Online]. Available: <https://advanced.onlinelibrary.wiley.com/doi/abs/10.1002/aenm.201904054>
- [33] D. Zhang, D. Li, Y. Hu, A. Mei, and H. Han, “Degradation pathways in perovskite solar cells and how to meet international standards,” *Communications Materials*, vol. 3, no. 1, p. 58, Aug. 2022. [Online]. Available: <https://doi.org/10.1038/s43246-022-00281-z>
- [34] S. Y. Kim, C. C. F. Kumachang, and N. Y. Doumon, “Characterization tools to probe degradation mechanisms in organic and perovskite solar cells,” *Solar RRL*, vol. 7, no. 13, p. 2300155, 2023. [Online]. Available: <https://onlinelibrary.wiley.com/doi/abs/10.1002/solr.202300155>
- [35] M. T. Neukom, A. Schiller, S. Züfle, E. Knapp, J. Ávila, D. Pérez-del Rey, C. Dreessen, K. P. Zanoni, M. Sessolo, H. J. Bolink, and B. Ruhstaller, “Consistent Device Simulation Model Describing Perovskite Solar Cells in Steady-State, Transient, and Frequency Domain,” *ACS Applied Materials & Interfaces*, vol. 11, no. 26, pp. 23 320–23 328, Jul. 2019. [Online]. Available: <https://pubs.acs.org/doi/10.1021/acsami.9b04991>
- [36] M. A. Torre Cachafeiro, E. L. Comi, S. Parayil Shaji, S. Narbey, S. Jenatsch, E. Knapp, and W. Tress, “Ion migration in mesoscopic perovskite solar cells: Effects on electroluminescence, open circuit voltage, and photovoltaic quantum efficiency,” *Advanced Energy Materials*, vol. 15,

- no. 5, p. 2403850, 2025. [Online]. Available: <https://advanced.onlinelibrary.wiley.com/doi/abs/10.1002/aenm.202403850>
- [37] W. Tress, J. P. Correa Baena, M. Saliba, A. Abate, and M. Graetzel, “Inverted current–voltage hysteresis in mixed perovskite solar cells: Polarization, energy barriers, and defect recombination,” *Advanced Energy Materials*, vol. 6, no. 19, p. 1600396, 2016. [Online]. Available: <https://advanced.onlinelibrary.wiley.com/doi/abs/10.1002/aenm.201600396>
- [38] G. Richardson, S. E. J. O’Kane, R. G. Niemann, T. A. Peltola, J. M. Foster, P. J. Cameron, and A. B. Walker, “Can slow-moving ions explain hysteresis in the current–voltage curves of perovskite solar cells?” *Energy Environ. Sci.*, vol. 9, pp. 1476–1485, 2016. [Online]. Available: <http://dx.doi.org/10.1039/C5EE02740C>
- [39] W. Tress, “Metal Halide Perovskites as Mixed Electronic–Ionic Conductors: Challenges and Opportunities—From Hysteresis to Memristivity,” *The Journal of Physical Chemistry Letters*, vol. 8, no. 13, pp. 3106–3114, Jul. 2017, publisher: American Chemical Society. [Online]. Available: <https://doi.org/10.1021/acs.jpcllett.7b00975>
- [40] O. Zbinden, E. Knapp, and W. Tress, “Identifying performance limiting parameters in perovskite solar cells using machine learning,” *Solar RRL*, vol. 8, no. 6, p. 2300999, 2024. [Online]. Available: <https://onlinelibrary.wiley.com/doi/abs/10.1002/solr.202300999>
- [41] A. These, L. J. A. Koster, C. J. Brabec, and V. M. Le Corre, “Beginner’s guide to visual analysis of perovskite and organic solar cell current density–voltage characteristics,” *Advanced Energy Materials*, vol. 14, no. 21, p. 2400055, 2024. [Online]. Available: <https://advanced.onlinelibrary.wiley.com/doi/abs/10.1002/aenm.202400055>
- [42] P. Calado, D. Burkitt, J. Yao, J. Troughton, T. M. Watson, M. J. Carnie, A. M. Telford, B. C. O’Regan, J. Nelson, and P. R. Barnes, “Identifying dominant recombination mechanisms in perovskite solar cells by measuring the transient ideality factor,” *Phys. Rev. Appl.*, vol. 11, p. 044005, Apr 2019. [Online]. Available: <https://link.aps.org/doi/10.1103/PhysRevApplied.11.044005>
- [43] L. Wang, Q. Miao, D. Wang, M. Chen, H. Bi, J. Liu, A. K. Baranwal, G. Kapil, Y. Sanehira, T. Kitamura, T. Ma, Z. Zhang, Q. Shen, and S. Hayase, “14.31 % power conversion efficiency of sn-based perovskite solar cells via efficient reduction of sn⁴⁺,” *Angewandte Chemie International Edition*, vol. 62, no. 33, p. e202307228, 2023. [Online]. Available: <https://onlinelibrary.wiley.com/doi/abs/10.1002/anie.202307228>
- [44] M. Azzouzi, P. Calado, A. M. Telford, F. Eisner, X. Hou, T. Kirchartz, P. R. F. Barnes, and J. Nelson, “Overcoming the limitations of transient photovoltage measurements for studying recombination in organic solar cells,” *Solar RRL*, vol. 4, no. 5, p. 1900581, 2020. [Online]. Available: <https://onlinelibrary.wiley.com/doi/abs/10.1002/solr.201900581>
- [45] J. Bisquert and M. Janssen, “From frequency domain to time transient methods for halide perovskite solar cells: The connections of imps, imvs, tpc, and tpv,” *The Journal of Physical Chemistry Letters*, vol. 12, no. 33, pp. 7964–7971, 2021.
- [46] M. Che, Y. Fang, J. Yuan, Y. Zhu, Q. Liu, and J. Song, “F-doped tio₂ compact film for high-efficient perovskite solar cells,” *International Journal of Electrochemical Science*, vol. 12, no. 2, pp. 1064–1074, 2017. [Online]. Available: <https://www.sciencedirect.com/science/article/pii/S1452398123105396>
- [47] J. Thiesbrummel, S. Shah, E. Gutierrez-Partida, F. Zu, F. Peña-Camargo, S. Zeiske, J. Diekmann, F. Ye, K. P. Peters, K. O. Brinkmann, P. Caprioglio, A. Dasgupta, S. Seo, F. A. Adeleye, J. Warby, Q. Jeangros, F. Lang, S. Zhang, S. Albrecht, T. Riedl, A. Armin, D. Neher, N. Koch, Y. Wu, V. M. Le Corre, H. Snaith, and M. Stollerfoht, “Ion-induced field screening as a dominant factor in perovskite solar cell operational stability,” *Nature Energy*, vol. 9, no. 6, pp. 664–676, Jun. 2024. [Online]. Available: <https://doi.org/10.1038/s41560-024-01487-w>
- [48] A. Guerrero, J. Bisquert, and G. Garcia-Belmonte, “Impedance spectroscopy of metal halide perovskite solar cells from the perspective of equivalent circuits,” *Chemical Reviews*, vol. 121, no. 23, pp. 14 430–14 484, 2021.

5 Supporting information

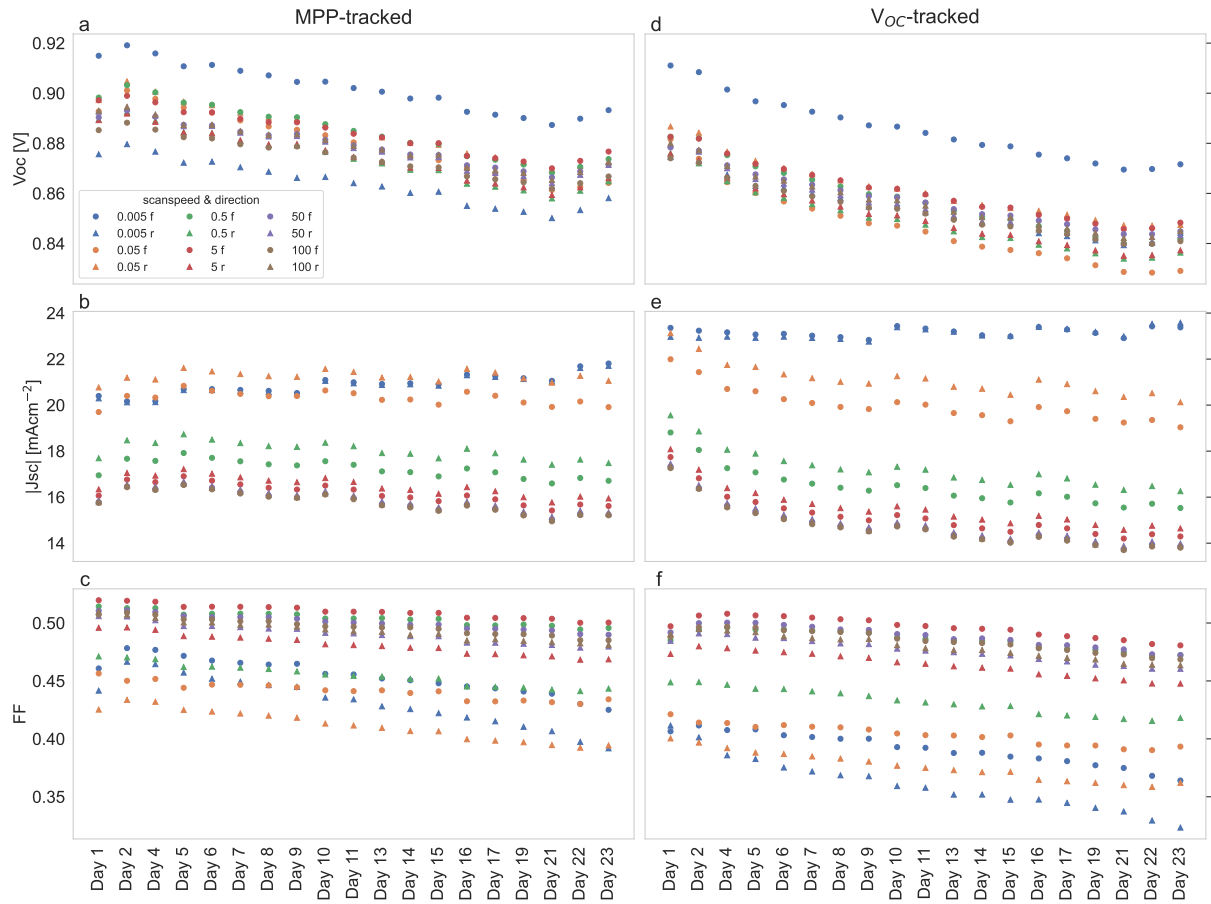


Figure 7: Complementary to Figure 3. a-c show the results for the device kept at MPP, d-f for the device kept at V_{OC} . a & d: V_{OC} . b & e: Absolute value of J_{SC} . c & f: FF.

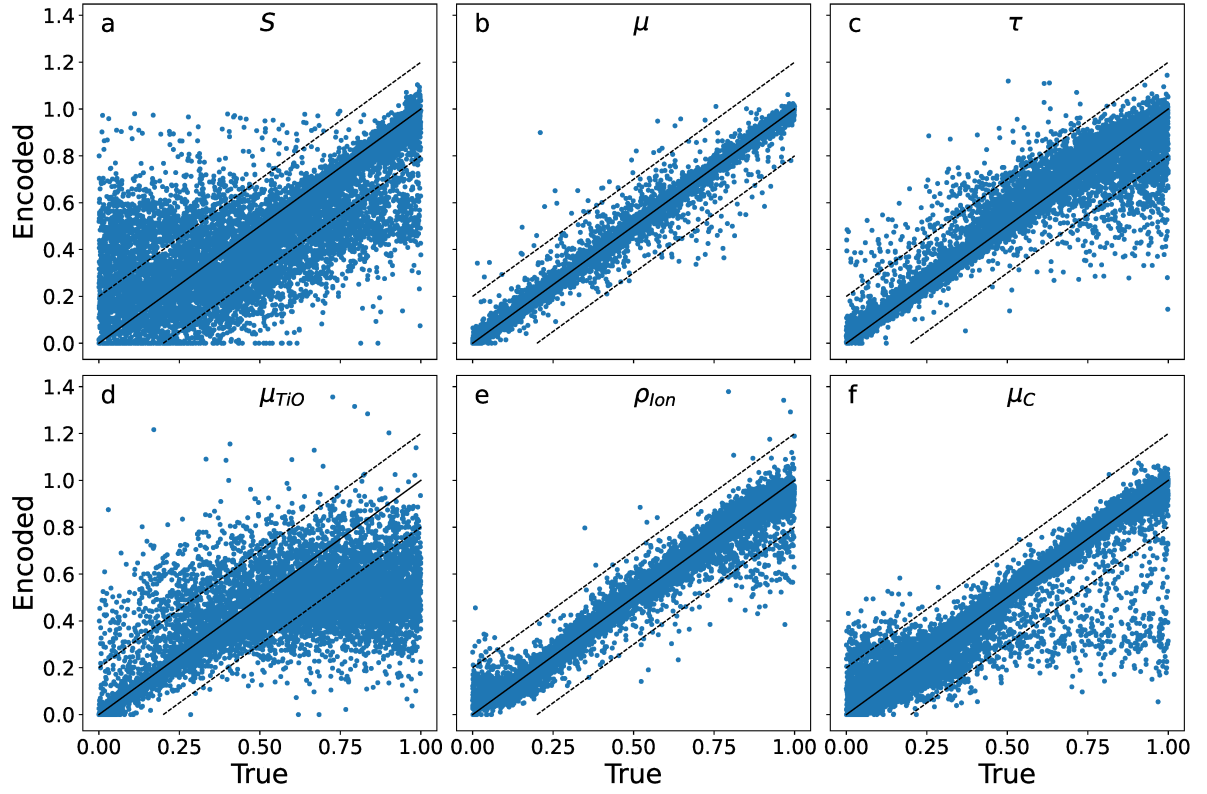


Figure 8: Log-normalized parameter estimates for the test set. a: S , b: μ , c: τ , d: μ_{TiO_2} , e: ρ_{Ion} , f: μ_C . The dashed lines indicate the boundaries of a confidence interval where the residuals are ≤ 0.2 .

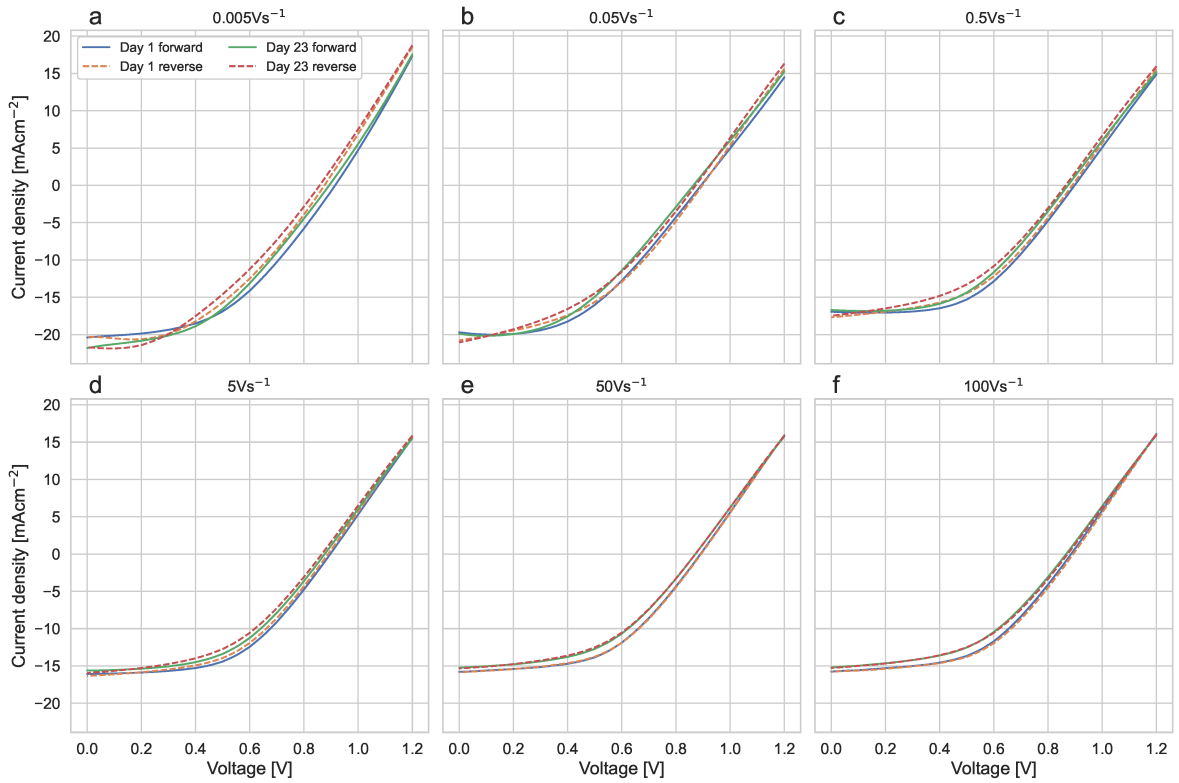


Figure 9: Comparison of the J-V curves by scan speed from the first and last day of the MPP-tracked device measured in the stability setup.

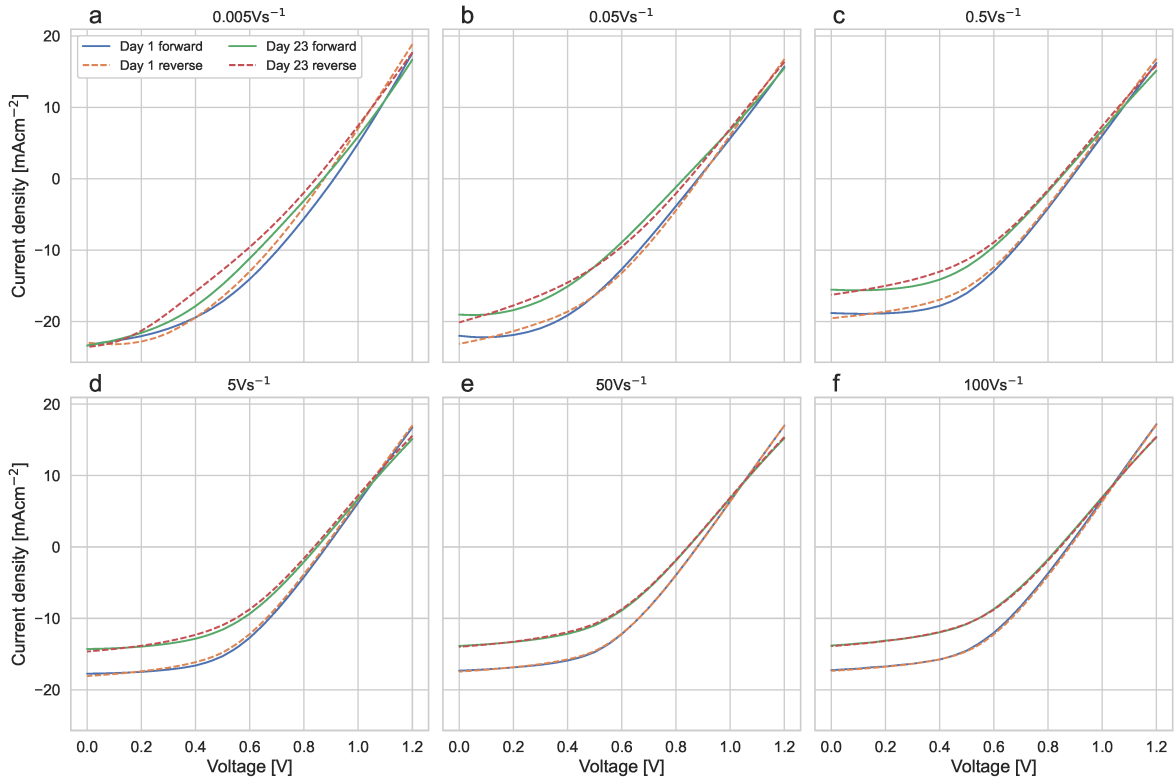


Figure 10: Comparison of the J-V curves by scan speed from the first and last day of the V_{OC} -tracked device measured in the stability setup.

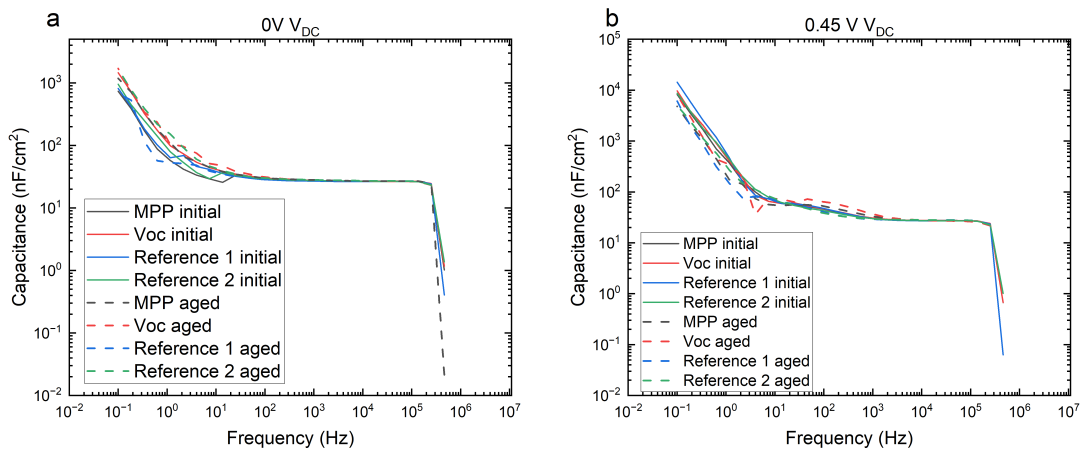


Figure 11: Capacitance vs frequency plot of cell in dark before and after aging, along with references. Electrochemical impedance spectroscopy (EIS) was conducted in the dark using the PAIOS system. A 10 mV AC perturbation was applied across a frequency range of 10 MHz to 0.1 Hz to characterize the frequency-dependent electrical response of the devices.

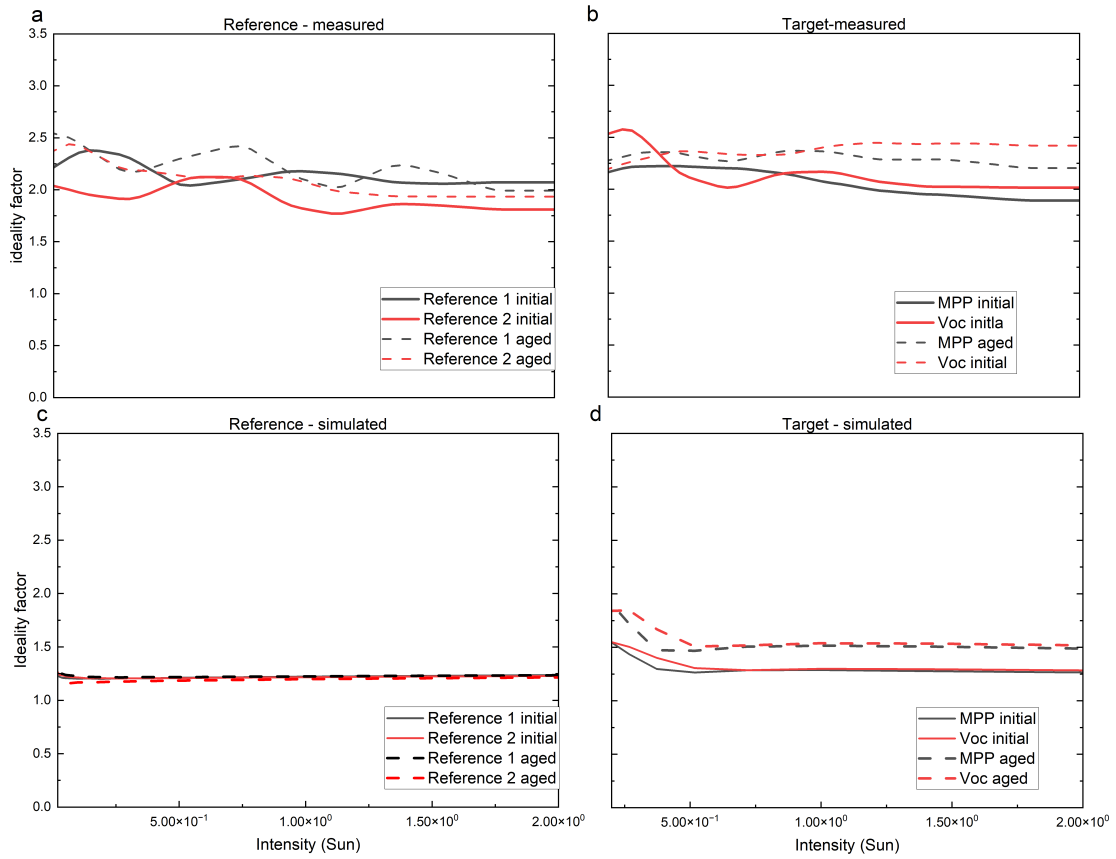


Figure 12: a,b shows the measured ideality factors of reference and stressed devices. c, d are the simulated ideality factors of the reference and stressed devices

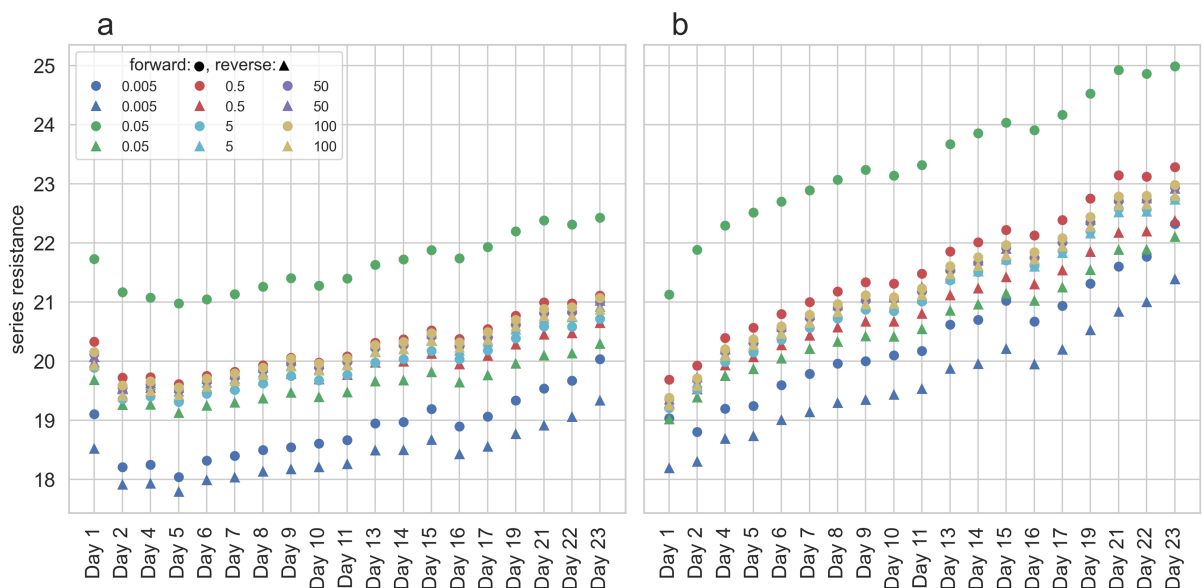


Figure 13: Differential series resistance between 0.8 V and 1 V for a: device kept at MPP, and b: device kept at V_{OC} , for each day, scan speed, and scanning direction.

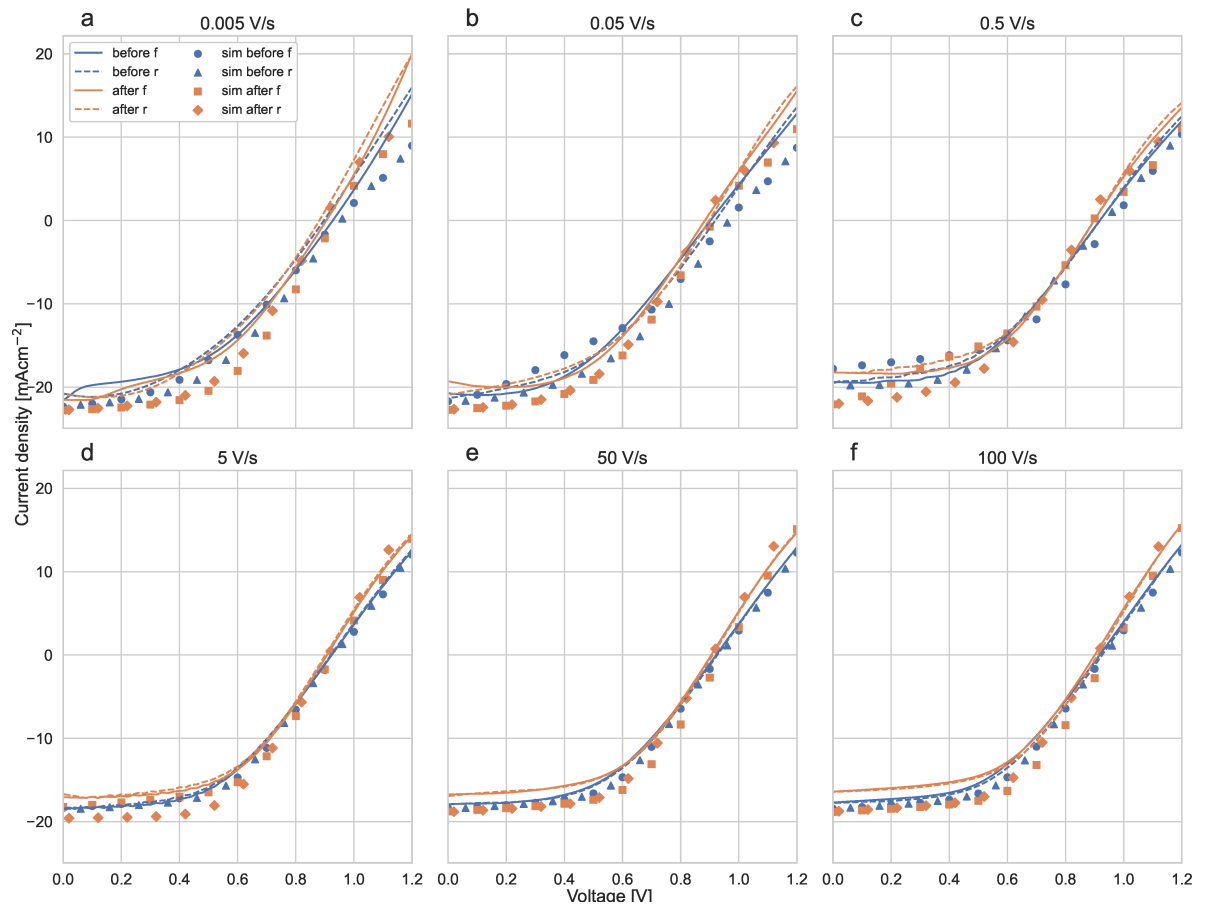


Figure 14: Measured J-V curves with Paios and simulation based on AE estimated parameters for the device kept at MPP before and after stressing.

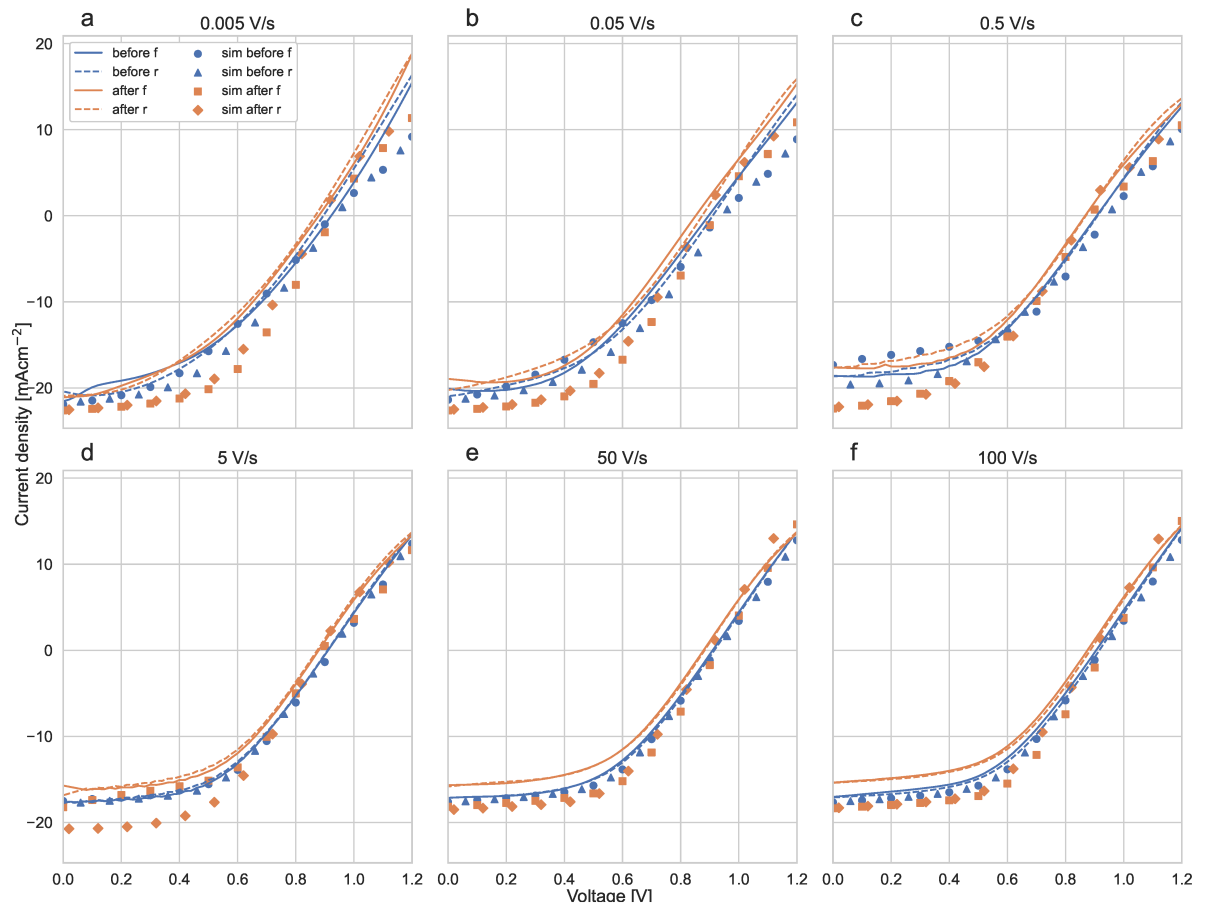


Figure 15: Measured J-V curves with Paicos and simulation based on AE estimated parameters for the device kept at V_{OC} before and after stressing.

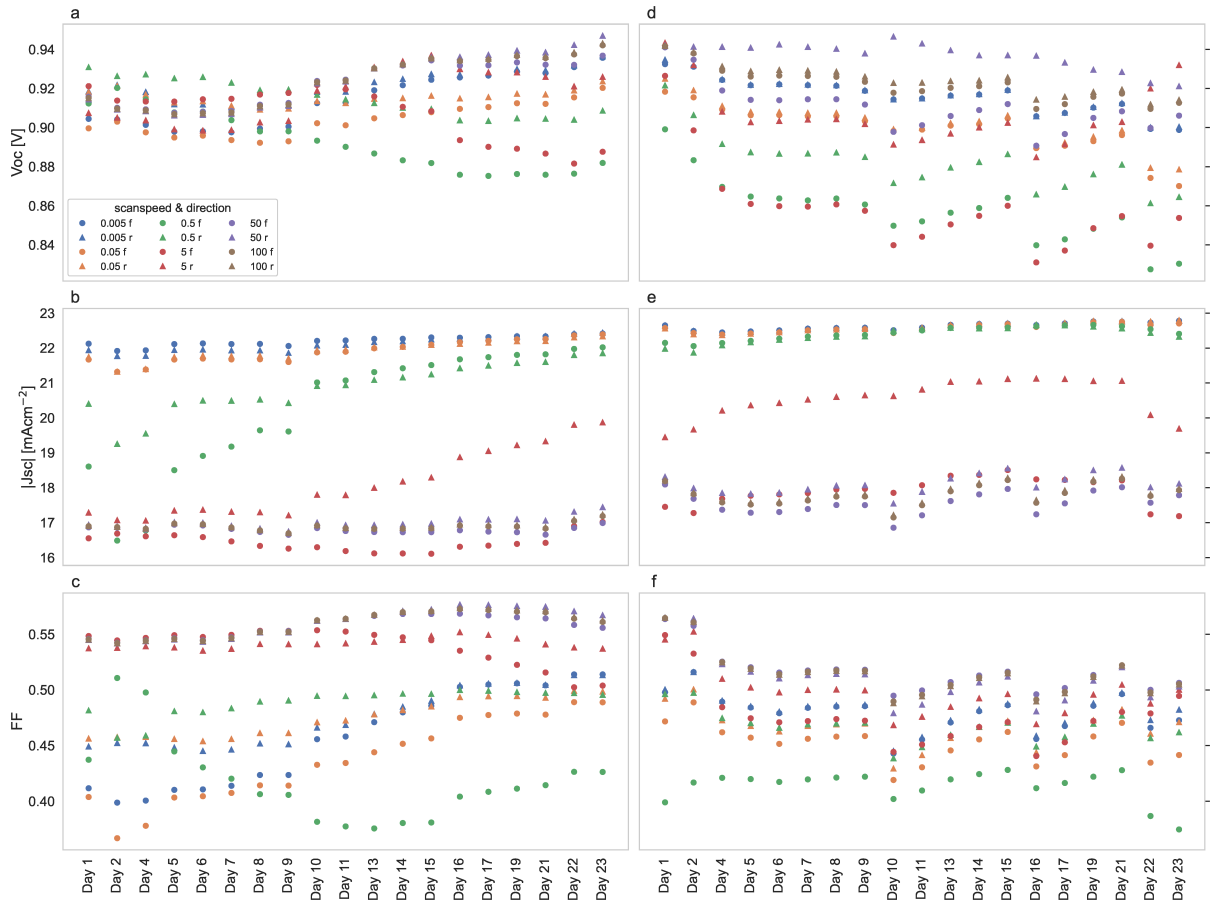


Figure 16: Evolution of key parameters extracted from simulations based on parameter estimates. a-c show the results for the device kept at MPP, d-f for the device kept at V_{OC} . a & d: V_{OC} . b & e: Absolute value of J_{SC} . c & f: FF.

Table 3: Complementary to Figure 5, the numeric values are listed in this table for both devices

		S [cms ⁻¹]	μ [cm ² V ⁻¹ s ⁻¹]	τ [ns]	μ_{TiO_2} [cm ² V ⁻¹ s ⁻¹]	μ_C [cm ² V ⁻¹ s ⁻¹]	ρ_{ion} [cm ⁻³]	
MPP-TRACKED	DAY 1	23.09	17.51	3.14	$7.81 \cdot 10^{-5}$	$2.16 \cdot 10^{-8}$	$2.51 \cdot 10^{17}$	
	DAY 2	20.73	21.76	2.45	$8.16 \cdot 10^{-5}$	$4.06 \cdot 10^{-8}$	$2.45 \cdot 10^{17}$	
	DAY 4	23.43	21.39	2.43	$8.56 \cdot 10^{-5}$	$3.44 \cdot 10^{-8}$	$2.47 \cdot 10^{17}$	
	DAY 5	25.81	23.28	2.36	$9.18 \cdot 10^{-5}$	$2.29 \cdot 10^{-8}$	$2.35 \cdot 10^{17}$	
	DAY 6	24.89	23.31	2.38	$8.73 \cdot 10^{-5}$	$2.05 \cdot 10^{-8}$	$2.41 \cdot 10^{17}$	
	DAY 7	26.92	22.11	2.44	$9.04 \cdot 10^{-5}$	$1.83 \cdot 10^{-8}$	$2.52 \cdot 10^{17}$	
	DAY 8	30.10	18.31	2.87	$9.55 \cdot 10^{-5}$	$1.58 \cdot 10^{-8}$	$2.62 \cdot 10^{17}$	
	DAY 9	29.96	16.96	2.94	$9.44 \cdot 10^{-5}$	$1.56 \cdot 10^{-8}$	$2.59 \cdot 10^{17}$	
	DAY 10	33.42	9.97	5.34	$9.87 \cdot 10^{-5}$	$1.02 \cdot 10^{-8}$	$2.36 \cdot 10^{17}$	
	DAY 11	34.75	9.41	5.72	$9.84 \cdot 10^{-5}$	$9.31 \cdot 10^{-9}$	$2.58 \cdot 10^{17}$	
	DAY 13	36.69	6.50	8.54	$9.45 \cdot 10^{-5}$	$7.75 \cdot 10^{-9}$	$2.75 \cdot 10^{17}$	
	DAY 14	39.56	5.15	10.73	$9.72 \cdot 10^{-5}$	$6.96 \cdot 10^{-9}$	$2.73 \cdot 10^{17}$	
	DAY 15	40.19	4.14	13.85	$9.31 \cdot 10^{-5}$	$6.53 \cdot 10^{-9}$	$2.89 \cdot 10^{17}$	
	DAY 16	49.68	2.53	22.38	$1.08 \cdot 10^{-4}$	$5.28 \cdot 10^{-9}$	$2.61 \cdot 10^{17}$	
	DAY 17	49.89	2.29	25.29	$1.03 \cdot 10^{-4}$	$4.75 \cdot 10^{-9}$	$2.77 \cdot 10^{17}$	
	DAY 19	48.27	2.10	28.39	$9.47 \cdot 10^{-5}$	$4.36 \cdot 10^{-9}$	$2.94 \cdot 10^{17}$	
	DAY 21	48.17	2.37	25.31	$9.09 \cdot 10^{-5}$	$3.96 \cdot 10^{-9}$	$3.12 \cdot 10^{17}$	
	DAY 22	52.62	1.10	58.77	$8.65 \cdot 10^{-5}$	$3.74 \cdot 10^{-9}$	$2.87 \cdot 10^{17}$	
	DAY 23	48.70	$8.55 \cdot 10^{-1}$	77.56	$7.84 \cdot 10^{-5}$	$4.03 \cdot 10^{-9}$	$2.62 \cdot 10^{17}$	
	V _{OC} -TRACKED	DAY 1	39.68	4.02	21.90	$7.65 \cdot 10^{-5}$	$1.09 \cdot 10^{-8}$	$1.52 \cdot 10^{17}$
		DAY 2	58.05	$7.57 \cdot 10^{-1}$	93.61	$9.58 \cdot 10^{-5}$	$7.19 \cdot 10^{-9}$	$1.61 \cdot 10^{17}$
		DAY 4	74.50	$1.73 \cdot 10^{-1}$	$4.41 \cdot 10^2$	$1.03 \cdot 10^{-4}$	$4.98 \cdot 10^{-9}$	$1.85 \cdot 10^{17}$
		DAY 5	79.51	$1.52 \cdot 10^{-1}$	$5.42 \cdot 10^2$	$1.02 \cdot 10^{-4}$	$4.56 \cdot 10^{-9}$	$2.03 \cdot 10^{17}$
DAY 6		79.39	$1.34 \cdot 10^{-1}$	$6.64 \cdot 10^2$	$9.51 \cdot 10^{-5}$	$4.71 \cdot 10^{-9}$	$2.03 \cdot 10^{17}$	
DAY 7		79.74	$1.49 \cdot 10^{-1}$	$6.32 \cdot 10^2$	$9.06 \cdot 10^{-5}$	$4.62 \cdot 10^{-9}$	$2.12 \cdot 10^{17}$	
DAY 8		81.70	$1.55 \cdot 10^{-1}$	$6.24 \cdot 10^2$	$8.77 \cdot 10^{-5}$	$4.77 \cdot 10^{-9}$	$2.01 \cdot 10^{17}$	
DAY 9		86.52	$1.59 \cdot 10^{-1}$	$6.16 \cdot 10^2$	$8.75 \cdot 10^{-5}$	$4.62 \cdot 10^{-9}$	$2.08 \cdot 10^{17}$	
DAY 10		$1.00 \cdot 10^2$	$7.44 \cdot 10^{-2}$	$6.16 \cdot 10^2$	$9.37 \cdot 10^{-5}$	$4.72 \cdot 10^{-9}$	$2.12 \cdot 10^{17}$	
DAY 11		99.38	$8.99 \cdot 10^{-2}$	$1.47 \cdot 10^3$	$9.00 \cdot 10^{-5}$	$4.79 \cdot 10^{-9}$	$2.07 \cdot 10^{17}$	
DAY 13		97.10	$1.18 \cdot 10^{-1}$	$1.12 \cdot 10^3$	$8.12 \cdot 10^{-5}$	$4.83 \cdot 10^{-9}$	$1.97 \cdot 10^{17}$	
DAY 14		95.68	$1.45 \cdot 10^{-1}$	$8.74 \cdot 10^2$	$7.89 \cdot 10^{-5}$	$4.95 \cdot 10^{-9}$	$1.91 \cdot 10^{17}$	
DAY 15		92.71	$1.64 \cdot 10^{-1}$	$7.55 \cdot 10^2$	$7.38 \cdot 10^{-5}$	$5.09 \cdot 10^{-9}$	$1.75 \cdot 10^{17}$	
DAY 16		$1.20 \cdot 10^2$	$9.54 \cdot 10^{-2}$	$1.69 \cdot 10^3$	$8.55 \cdot 10^{-5}$	$4.19 \cdot 10^{-9}$	$2.46 \cdot 10^{17}$	
DAY 17		$1.15 \cdot 10^2$	$1.16 \cdot 10^{-1}$	$1.33 \cdot 10^3$	$8.20 \cdot 10^{-5}$	$4.52 \cdot 10^{-9}$	$2.37 \cdot 10^{17}$	
DAY 19		$1.07 \cdot 10^2$	$1.71 \cdot 10^{-1}$	$8.44 \cdot 10^2$	$7.61 \cdot 10^{-5}$	$4.99 \cdot 10^{-9}$	$2.26 \cdot 10^{17}$	
DAY 21		$1.03 \cdot 10^2$	$2.28 \cdot 10^{-1}$	$5.71 \cdot 10^2$	$7.24 \cdot 10^{-5}$	$4.96 \cdot 10^{-9}$	$2.11 \cdot 10^{17}$	
DAY 22		$1.16 \cdot 10^2$	$1.30 \cdot 10^{-1}$	$1.17 \cdot 10^3$	$8.70 \cdot 10^{-5}$	$6.45 \cdot 10^{-9}$	$2.97 \cdot 10^{17}$	
DAY 23		$1.08 \cdot 10^2$	$1.63 \cdot 10^{-1}$	$9.22 \cdot 10^2$	$8.34 \cdot 10^{-5}$	$8.16 \cdot 10^{-9}$	$3.07 \cdot 10^{17}$	